Optical Engineering

OpticalEngineering.SPIEDigitalLibrary.org

Fiber Bragg gratings as transient thermal gradient sensors

Drew A. Hackney
Kara J. Peters
Richard J. Black
Joannes M. Costa
Behzad Moslehi

SPIE.

Drew A. Hackney, Kara J. Peters, Richard J. Black, Joannes M. Costa, Behzad Moslehi, “Fiber Bragg gratings as transient thermal gradient sensors,” *Opt. Eng.* **55**(11), 114102 (2016), doi: 10.1117/1.OE.55.11.114102.

Optical Engineering 55(11), 114102 (November 2016)

Fiber Bragg gratings as transient thermal gradient sensors

Drew A. Hackney,[a] **Kara J. Peters,**[a,*] **Richard J. Black,**[b,*] **Joannes M. Costa,**[b] **and Behzad Moslehi**[b]
[a]North Carolina State University, Department of Mechanical and Aerospace Engineering, Campus Box 7910, Raleigh, North Carolina 27695, United States
[b]Intelligent Fiber Optic Systems Corporation, 2363 Calle Del Mundo, Santa Clara, California 95054, United States

Abstract. We experimentally subject a fiber Bragg grating to an unknown, variable temperature gradient. We use the full-spectral response of the grating to determine the magnitude of the gradient over the length of the grating via the full width at quarter maximum bandwidth. The experimental bandwidth and spectrum deformation were compared with a numerical model consisting of an analytical heat transfer model, a finite element analysis model, and the transfer matrix (T-matrix) method. The numerical model showed excellent agreement with the experimental results when the T-matrix method was modified to include the slope of the gradient in addition to the magnitude of the gradient. [DOI: 10.1117/1.OE.55.11.114102]

Keywords: fiber Bragg grating; full spectrum; temperature gradient; transfer matrix method.

Paper 160546 received Apr. 13, 2016; accepted for publication Oct. 18, 2016; published online Nov. 16, 2016.

1 Introduction

Fiber Bragg grating (FBG) sensors have a unique feature in that their response is not only sensitive to changes in strain and temperature, but also to changes in strain and temperature gradients. When FBGs are exposed to high temperature or strain gradients over their length, the reflected spectrum of the FBG is distorted, resulting in a bandwidth change. This bandwidth change can be distinguished from wavelength shifts due to average strain or temperature fields. Hill and Eggleton[1] first applied a nonuniform strain over the length of an FBG and observed the spectral deformation. The spectral deformation due to strain gradients has been commonly applied to identify damage in composite laminates.[2–5]

Measurements of FBG spectral bandwidth changes due to temperature gradients are not as prevalent due to the severity of the temperature gradients that would be required to develop a measurable change in the bandwidth of the reflected spectrum. It is, however, critical to measure temperature gradients in some high-temperature systems such as ablative thermal protection systems or jet engines.[6–10] While it is sometimes possible to measure thermal gradients with multiple FBGs[6–8] each of which is perpendicular to the gradient, in some cases it is more convenient or limited space requires one to have the FBGs parallel to the gradient. Thermocouples can measure average temperatures only across the gage length.

Researchers have created thermal gradients along the lengths of FBGs to increase the bandwidth to produce dispersion compensators. Lauzon et al.,[11] by setting an optical fiber with a written FBG in a 250-μm deep V-groove machined into a brass plate spanning two temperature controllers, obtained a temperature difference of 26.1°C. Chen et al.[12] produced a thermal gradient over the length of an FBG by encasing the FBG in a metal sleeve and wrapping the sleeve in a heating wire. Similarly, Eggleton et al.[13] and Rogers et al.[14] wrapped the optical fiber in a thin metal film that could be electrically heated, producing a maximum temperature difference of 150°C.

In contrast to these previous works, the goal of this paper is to apply a pure thermal gradient along the FBG gage length, without induced mechanical strain, to calibrate its bandwidth response to pure thermal gradients. In this work, an FBG is supported in a partition between two thermal baths of different temperatures. As the baths heat and cool toward ambient temperature, the thermal gradient along the FBG changes. The experimental measurements are validated with modeling of the heat transfer of the system and the resulting FBG response.

2 Experimental Setup

To force a temperature gradient over the length of an FBG, a container was constructed of polytetrafluoroethylene (PTFE, Teflon®). A schematic of the container is given in Fig. 1. PTFE was chosen because it has a similar thermal conductivity to the silica of the optical fiber and a broad operating temperature range of −73°C to 260°C, during which the material maintains its shape and function. This temperature range exceeds the temperature loads to be induced in this experiment. It is also easily machinable. The walls, ends, and center partition of the container were joined using a clear silicone caulk with an operating temperature range of −51°C to 204°C, also beyond the temperature range to be applied. The container included a partition located at the halfway point of its length that split the container into two equally sized compartments. The partition was 1-cm thick, the same thickness of the FBG. The compartments were filled with water at different temperatures, T_H and T_C. A small, 0.0254 cm, diameter hole was drilled into both ends and the center partition. The hole allows for an optical fiber to pass through the walls while remaining small enough to prevent water escaping the two

---

*Address all correspondence to: Kara J. Peters, E-mail: kjpeters@ncsu.edu; Richard J. Black, E-mail: rjb@ifos.com

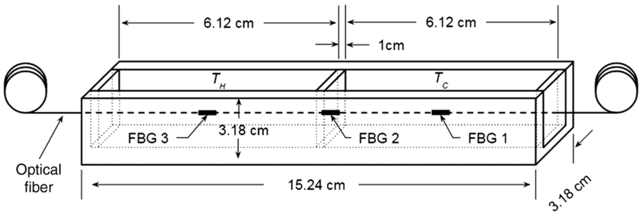

Fig. 1 Diagram showing the dimensions and configuration of the thermal gradient experiment using two different fluid baths separated by a central partition.

compartments. No bonding agents were used to hold the fiber in place.

To induce a temperature gradient, one compartment was filled with boiling water and the second compartment was filled with ice water. Over time, the temperature of the water in both baths cools or heats, respectively, to room temperature. To reduce the rate of temperature change in both baths, a thin layer of low-density polyethylene (LDPE) was wrapped around the upper surface of the container to insulate the fluid in the two compartments from the surrounding air. The LDPE layer reduced, but did not prevent heat transfer between the water baths and the lab environment. Reducing the heat transfer between the water baths and the lab environment allowed for a more consistent temperature load between the baths and the FBG in the partition; however, because the temperature of the baths was still variable, different thermal gradients were measured across the FBG during the experiment.

Optical fibers containing three FBGs were spliced together to form a single sensor array as shown in Fig. 1. One FBG was located in each bath to measure its temperature over time, and the third FBG was placed in the small diameter hole in the center partition. The FBGs used in the test have an operating temperature range of −40°C to 120°C, an initial full width at half maximum (FWHM) bandwidth of 0.25 ± 0.05 nm, a peak reflectivity of greater than 70%, a thermal response of approximately 9.9 pm/°C, and were 1 cm in length, which is the same length as the thickness of the partition. The FBG located in the partition was used to measure the temperature gradient through the PTFE partition.

3 Experimental Results

Table 1 gives the designation of each FBG, its location in the experiment, and its initial wavelength. As the baths were being filled, FBG 2 remained exposed to the laboratory environment outside the container. Once the baths were filled and covered with a layer of LDPE, an initial spectrum was recorded using a laboratory FBG interrogator, with FBG 2 remaining in the lab environment, and is plotted in Fig. 2. The reflectivity of the spectrum is normalized between 0 and 1, where 0 is defined as the global minimum of the spectrum and 1 is the global maximum of the spectrum. The decrease in maximum reflectivity between the sensors is due to splice losses as the FBGs were not originally written on the same optical fiber. The data from the initial spectrum were used to determine the baseline bandwidth for FBG 2. Once data collection was begun, FBG 2 was moved into the partition between the two baths. The dimensions of the FBG array were reduced in Fig. 1 for esthetic purposes. The FBGs were separated by 1.5 m, which required the fiber to loop in and out of the test fixture. This distance between FBGs allowed for each individual FBG to be moved and repositioned without affecting the position of the other two. When the section of the fiber containing FBG 2 was pulled into the test fixture, it was pulled through the cold bath, past the section of fiber containing FBG 1. Due to the small diameter of the optical fiber, there were no residual temperature effects of FBG 2 being pulled through the cold bath. The temperature measured by FBG 2 was influenced by the direct surroundings of FBG 2. The second reflected spectrum was recorded after 15 s, and successive spectra were recorded at 5-s intervals for a total of 10 min.

Table 1 Specifications of the three FBGs in the multiplexed array.

FBG	Location	Initial Bragg wavelength at 23°C (nm)	FWHM bandwidth for uniform temperature (nm)	FWQM bandwidth for uniform temperature (nm)	Peak reflectivity
1	Cold bath	1536.05	0.25	0.32	0.99
2	Partition	1560.23	0.25	0.32	0.8
3	Hot bath	1573.90	0.25	0.32	0.7

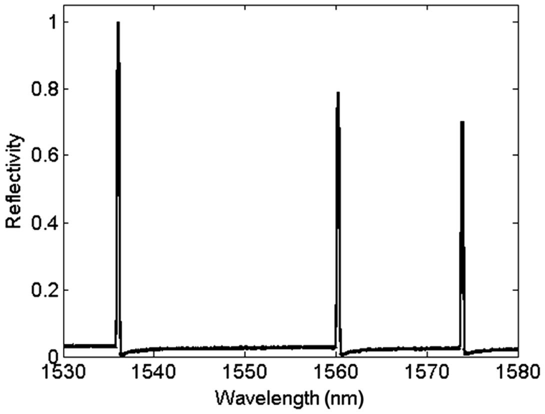

Fig. 2 Initial reflected spectrum of the 3-FBG array.

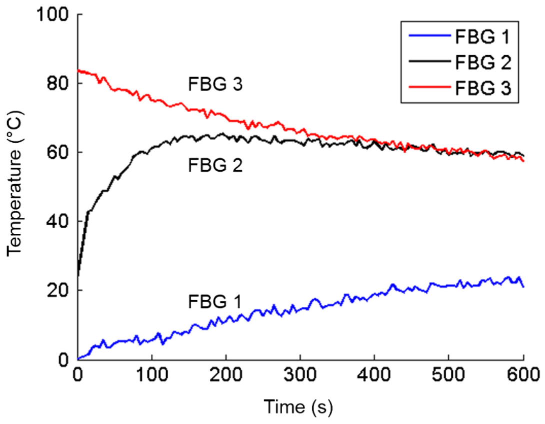

Fig. 3 Temperature response of all three FBGs during the experiment.

Figure 3 shows the temperature responses of FBG 1, FBG 2, and FBG 3 measured over the duration of the experiment. The temperature was calculated from the measured peak wavelength shift of the reflected spectrum for each FBG in the array using the calibration equation given in the following equation:

$$T = (-2.2455\times 10^{7}\,^\circ\mathrm{C})\left(\frac{\Delta\lambda}{\lambda}\right)^{2} + (1.6389\times 10^{5}\,^\circ\mathrm{C})\left(\frac{\Delta\lambda}{\lambda}\right) + 22.778^\circ\mathrm{C}. \tag{1}$$

Equation (1) was previously calibrated[15] over a wide temperature range (room temperature to 200°C) for an FBG sensor manufactured using an identical process to those in the 3-FBG array used in this paper. To lowest order, the temperature change is $\Delta T \approx 1.6\times 10^{5}\,^\circ\mathrm{C}(\Delta\lambda/\lambda)$ as in the companion paper.[8] To second order, the detailed fit of Eq. (1) is dependent on the calibration range and manufacturing process for the FBGs.

The temperature of FBG 2 initially changed more rapidly due to the smaller thermal mass of the partition, as compared with the baths. Due to its location within the PTFE partition, the temperature response of FBG 2 changed little after 150 s, compared with FBG 1 and FBG 3. After 350 s, the temperatures registered by FBG 2 and FBG 3 are within 1°C of each other, and at 530 s, the temperature of FBG 3 is warmer than the temperature of FBG 3. The temperature of the cold bath is above 20°C after approximately 420 s, and consistently within 1°C to 23°C (room temperature) after 515 s. While there is still an obvious difference in the temperature between the two baths after 300 s, the temperature of FBG 2 follows that of the hot bath. This is likely due to the thermal load produced by the hot bath conducting through the center partition and the thermal load from the cold bath being too weak to counter the load from the hot bath. Numerical simulations of this effect will be presented later. At 350 s, FBGs 2 and 3 are outputting same temperature values, and by 400 s, it is possible that the temperature of the partition is equal to the temperature of the hot bath through the thickness of the partition. Therefore, no significant temperature gradient was applied to FBG 2 and the experiment was stopped after 600 s.

The full width at half maximum (FWHM) and full width at quarter maximum (FWQM) bandwidths were calculated for FBG 2 over the duration of the experiment and are shown in Fig. 4. The FWHM bandwidth is the classically used measurement when determining the bandwidth of an FBG reflected spectrum; however, given a Gaussian shaped spectrum, the FWHM is an arbitrary parameter and does not inherently provide more or less information than the FWQM bandwidth. For the spectra observed in the experiment, the FWQM bandwidth displays a more obvious contrast to the initial bandwidth of the spectrum. Also, at 330 s, the magnitude of the FWHM bandwidth of FBG 2 returns to within 5% of its initial value. Given the noise present in the data, this can be considered the bandwidth measurement limit. The FWQM bandwidth returns to within 5% of its initial value after 435 s, providing measurement sensitivity over a wider temperature gradient range. There is no significant deformation in the spectrum from its initial Gaussian shape so the information presented by the FWQM bandwidth is equally valid to that of the FWHM bandwidth. The goal of this work is to demonstrate a relationship between the bandwidth of the FBG spectrum and the temperature gradient applied across the FBG gage length, and therefore the FWQM was used.

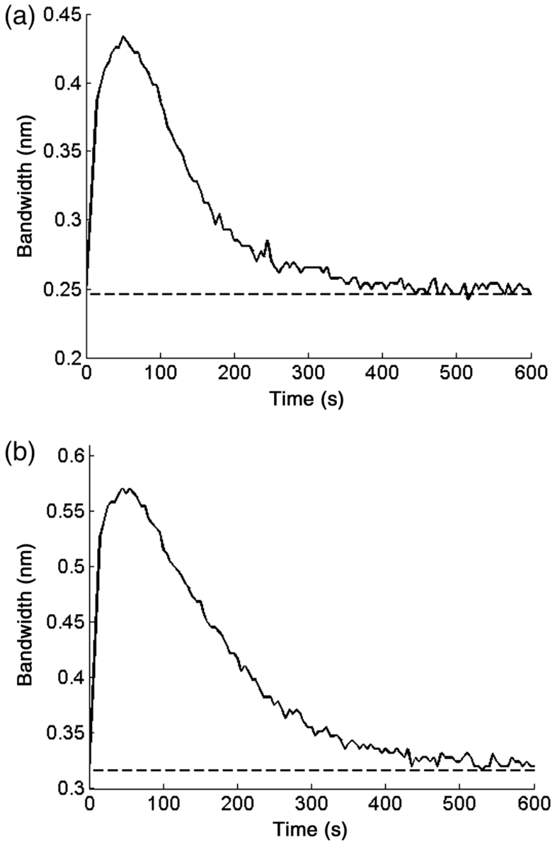

Fig. 4 The (a) FWHM and (b) FWQM bandwidths of FBG 2 during the experiment. The horizontal dashed line represents the initial bandwidth.

The bandwidth and reflectivity of an FBG have a roughly inverse relationship. The maximum reflectivity of FBG 2 is overlaid with the FWQM of FBG 2 in Fig. 5 to show that the expected inverse relationship between maximum reflectivity and bandwidth was observed. Generally, the reflectivity information is not reliable for sensing applications since it

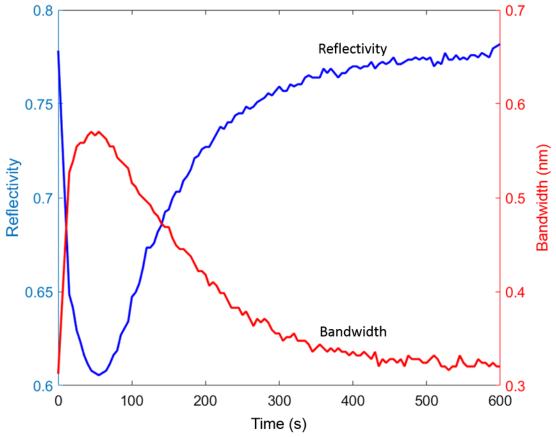

Fig. 5 Maximum reflectivity of FBG 2 during the experiment plotted on the same axis as the FWQM bandwidth.

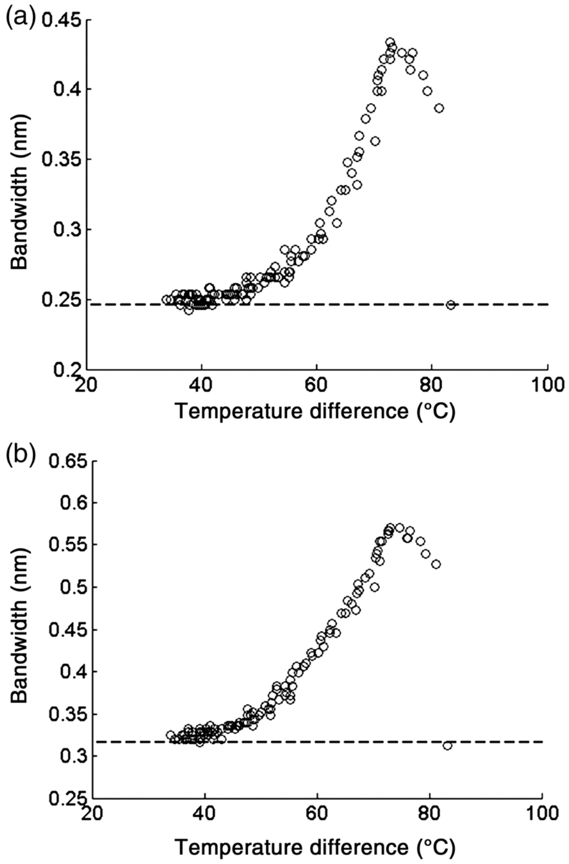

Fig. 6 The (a) FWHM and (b) FWQM bandwidths of FBG 2 plotted against the temperature difference of FBG 1 and FBG 3.

is highly sensitive to laser power and bending loss fluctuations in the optical fiber.

Figure 6 shows a scatter plot of the FWHM and FWQM bandwidths of FBG 2 as a function of the temperature difference between FBG 3 and FBG 1. The dashed line on each plot represents the initial FWHM or FWQM of FBG 2. The bandwidth behaves as expected for most of the temperature difference range, but, however, peaks at approximately 75°C. This behavior was not explained by modeling of a simple linear temperature gradient across the FBG gage length, but instead requires a more detailed modeling of the heat transfer between the two baths and through the partition thickness. This modeling should capture the heat transfer through the partition, the applied thermal loading to the FBG gage length due to the heat transfer, and finally the two-mode coupling along the FBG length in the presence of a varying temperature field, which determines the reflected spectrum. These components of the simulation will be presented in the following sections.

4 Numerical Model

A numerical simulation of the experiment was performed to verify that the measured bandwidth gradients of the FBG in the center partition were in fact due to the applied thermal gradient. The numerical model consisted of three components: a two-dimensional (2-D) analytical heat transfer model of the entire system, a detailed finite element model of the center partition, and a modified transfer matrix (T-matrix) model of the FBG optical response. The analytical heat transfer model calculated the wall temperatures on the hot and cold sides of the partition given the experimentally observed bath temperatures. The wall temperatures were then input into the finite element model which calculated the temperature profile through the thickness of the partition. Finally, the modified T-matrix method was used to calculate numerically determined reflected spectra of FBG 2 subjected to the temperature profile determined by the ANSYS model over its length.

4.1 *Analytical Heat Transfer Model of System*

A schematic of the analytical heat transfer model of the system is shown in Fig. 7 and covers the two baths and the center PTFE partition between them. The heat transfer consists of convection on the hot and cold walls of the center partition and conduction through the thickness of the partition. The red and blue lines denote the hot and cold sides of the partition, respectively.

The heat transfer of the system can be mathematically described using the following equation:

$$h_h(T_h - T_{hw}) = \frac{k(T_{hw} - T_{cw})}{L} = h_c(T_{wc} - T_c), \tag{2}$$

where T_h and T_c are the temperatures of the hot and cold baths, respectively, T_{hw} and T_{cw} are the temperatures of the hot and cold walls, h_h and h_c are the convective heat transfer coefficients along the hot and cold walls, L is the length of the partition, and k is the thermal conductivity of the PTFE of the partition. T_h and T_c are calculated from a polynomial fit to the experimental data from FBG 1 and FBG 3 of Fig. 4. These fits are given in Eqs. (3) and (4) for the hot and cold baths, respectively:

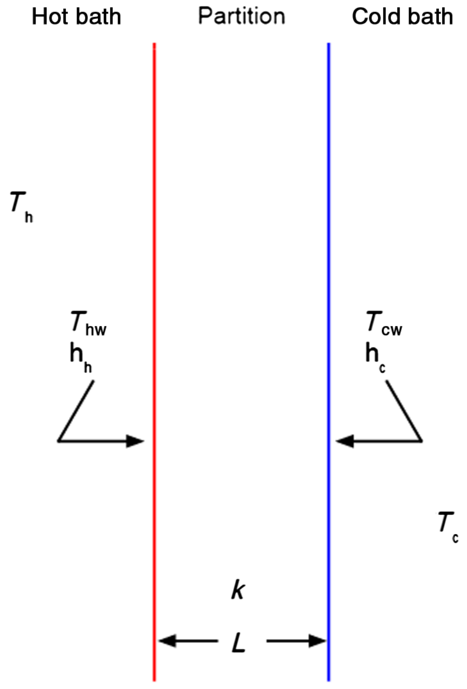

Fig. 7 Schematic of the 2-D analytical heat transfer model.

$$T_h = -\left(9.9987\times 10^{-8}\,\frac{^\circ\mathrm{C}}{\mathrm{s}^3}\right)t^3 + \left(1.4346\times 10^{-4}\,\frac{^\circ\mathrm{C}}{\mathrm{s}^2}\right)t^2 + 0.09235\,\frac{^\circ\mathrm{C}}{\mathrm{s}}\,t + 83.8444^\circ\mathrm{C}, \tag{3}$$

$$T_c = \left(4.4906\times 10^{-11}\,\frac{^\circ\mathrm{C}}{\mathrm{s}^4}\right)t^4 - \left(1.9869\times 10^{-7}\,\frac{^\circ\mathrm{C}}{\mathrm{s}^3}\right)t^3 + \left(3.4420\times 10^{-5}\,\frac{^\circ\mathrm{C}}{\mathrm{s}^2}\right)t^2 + 0.04152\,\frac{^\circ\mathrm{C}}{\mathrm{s}}\,t + 1.9120^\circ\mathrm{C}. \tag{4}$$

Equation (2) can be split into two equations to solve for the two unknowns, T_{hw} and T_{cw}:

$$T_{hw} = \frac{T_h h_h(k + h_c L) + T_c h_c k}{h_h(k + h_c L) + h_c k}, \tag{5}$$

$$T_{cw} = \frac{T_c h_c(k + h_h L) + T_h h_h k}{h_c(k + h_h L) + h_h k}. \tag{6}$$

Equations (2)–(6) assume a linear temperature gradient through the thickness of the PTFE partition, the validity of which will be checked later.

The convective heat transfer coefficients, h_h and h_c, are not constant, but they depend on a combination of the Rayleigh number (Ra) of the fluid, the temperature difference between the wall and the fluid, the thermal conductivity of the fluid, and the Prandtl number (Pr). For laminar flow ($Ra < 10^9$), a vertical plate with submerged length L_p, the convective heat transfer coefficient can be calculated using the following equation:[16]

$$h = \frac{k}{L_p}\left\{0.68 + \frac{0.67 Ra_L^{1/4}}{\left[1 + \left(\frac{0.492}{Pr}\right)^{9/16}\right]^{4/9}}\right\}. \tag{7}$$

Assuming the center partition is fully submerged, L_p is 0.03175 m. The Rayleigh number is calculated using Eqs. (8) and (9) for the hot and cold walls.

$$Ra_h = \frac{g\alpha}{k_\nu \phi}(T_h - T_{hw})L_p^3, \tag{8}$$

$$Ra_c = \frac{g\alpha}{k_\nu \phi}(T_{cw} - T_c)L_p^3, \tag{9}$$

where g is the acceleration due to gravity, α is the thermal expansion coefficient, k_ν is the kinematic viscosity, and ϕ is the thermal diffusivity. The value of $g\alpha/(k_\nu\phi)$ for water is temperature dependent and can be estimated using the following equation:[16]

$$\frac{g\alpha}{k_\nu \phi} = (8.44^\circ\mathrm{C}^{-2})T^2 + (590^\circ\mathrm{C}^{-1})T. \tag{10}$$

Given the values of $g\alpha/(k_\nu\phi)$ over the temperature range of 0°C to 100°C, the temperature difference between the PTFE surface and the fluid bath, and L_p, Ra never approaches 10^9, so the laminar flow calculation for h presented in Eqs. (5) and (6) holds. The Prandtl number for water is also temperature dependent and can be estimated using the following equation:[16]

$$Pr = (2.92\times 10^{-7\circ}\mathrm{C}^{-4})T^4 - (7.97\times 10^{-5\circ}\mathrm{C}^{-3})T^3 + (8.42\times 10^{-3\circ}\mathrm{C}^{-2})T^2 + (0.452^\circ\mathrm{C}^{-1})T + 13.3. \tag{11}$$

Finally, the thermal conductivity of water depends on temperature and can be described by the following equation:[16]

$$k = \left(-7.88\times 10^{-6}\,\frac{\mathrm{W}}{\mathrm{m}^\circ\mathrm{C}^3}\right)T^2 - \left(1.98\times 10^{-3}\,\frac{\mathrm{W}}{\mathrm{m}^\circ\mathrm{C}^2}\right)T + 0.559\,\frac{\mathrm{W}}{\mathrm{m}^\circ\mathrm{C}}. \tag{12}$$

Equations (8)–(12) were used to calculate the unknown variables in Eq. (7), which was used to calculate h_h and h_c. The values of h_h and h_c were then used to calculate T_{hw} and T_{cw} in Eqs. (5) and (6), respectively. A comparison between the temperatures of the baths and the wall temperatures is shown in Fig. 8. This figure shows that, in the beginning of the test, the temperature of the hot wall is approximately 20°C cooler than that of the hot bath. By the end of the test, the difference in temperature between the hot bath and the hot side of the PTFE partition is reduced to approximately 10°C. Initially, the cold wall is significantly warmer than the cold bath due to a combination of lower h_c values and temperature conduction through the PTFE partition. Due to the conduction through the PTFE, the cold bath never drops below room temperature.

Polynomial expressions were fit to the calculated hot and cold wall temperatures and were input into the finite element model of the partition as the temperature loads for the hot and cold walls:

$$T_{hws} = -\left(3.45\times 10^{-5}\,\frac{\mathrm{C}}{s^2}\right)t^2 - \left(5.04\times 10^{-2}\,\frac{\mathrm{C}}{s^2}\right)t + 65.6^\circ\mathrm{C}, \tag{13}$$

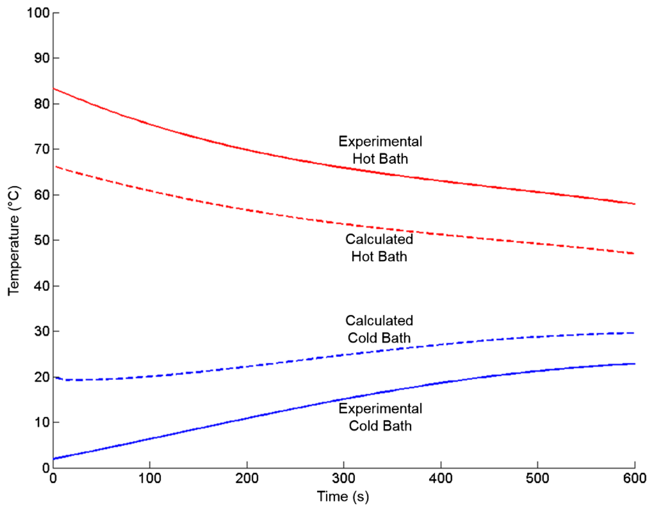

Fig. 8 Comparison of the hot and cold bath experimental temperatures and the calculated wall temperatures.

$$T_{cws} = -\left(9.02\times10^{-8}\,\frac{\mathrm{C}}{s^3}\right)t^3 + \left(7.67\times10^{-5}\,\frac{\mathrm{C}}{s^2}\right)t^2 + \left(3.64\times10^{-3}\,\frac{\mathrm{C}}{s}\right)t + 19.1^\circ\mathrm{C}. \tag{14}$$

4.2 *Finite Element Model of Center Partition*

The geometry of the finite element model represents a cross-section of the partition with dimensions 3.175 cm by 1 cm and was implemented in ANSYS. A 2-D model was sufficient as the optical fiber was located far from the outer PTFE walls. Bisecting the model geometry was a 0.0125-cm thick strip used to numerically represent the silica optical fiber. The material properties used for the PTFE are given in Table 2. The material properties for the silica used in the model are given in Table 3. Unlike for PTFE, the thermal conductivity of silica varies across the expected temperature range as plotted in Fig. 9. The model was meshed with 8-node, 2-D thermal (Plane77) elements. The meshed model geometry is shown in Fig. 10. The curve fits for the hot and cold wall temperatures in Eqs. (13) and (14), respectively, were applied to the left and right sides of the ANSYS model.

All nodes were set to an initial temperature of 23°C, and a 600-s long transient analysis was conducted in ANSYS. The time-dependent temperatures at 21 nodes in 0.05-cm increments along the silica strip were recorded at each time interval. The temperature profiles of 11 of these nodes, with a spacing of 0.1 cm, taken at 5-s intervals during the analysis are shown in Fig. 11. This figure shows that the temperature profile through the thickness of the partition is not linear for the first 100 s of the model. However, the analytical model used to calculate the wall temperatures assumed a linear temperature profile through the thickness of the partition

Table 2 PTFE material properties used in the numerical finite element model.[16]

Material property	Value
Density (ρ)	2200 $\mathrm{kg\,m^{-3}}$
Specific heat (c_p)	1040 $\mathrm{J\,kg^{-1}\,K^{-1}}$
Thermal conductivity (k)	0.245 $\mathrm{W\,m^{-1}\,K^{-1}}$

Table 3 Material properties for density and specific heat for silica used in the numerical ANSYS model.[16]

Material property	Value
Density (ρ)	2210 $\mathrm{kg\,m^{-3}}$
Specific heat (c_p)	730 $\mathrm{J\,kg^{-1}\,K^{-1}}$

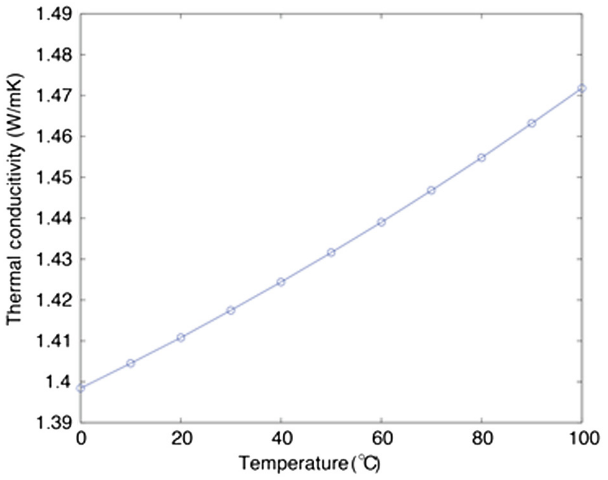

Fig. 9 Temperature-dependent thermal conductivity for silica.[17]

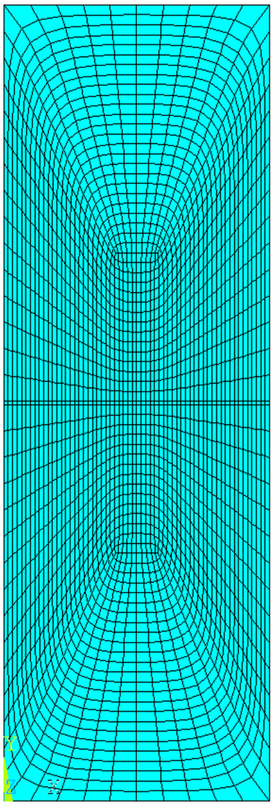

Fig. 10 Meshed model geometry used in the numerical finite element model.

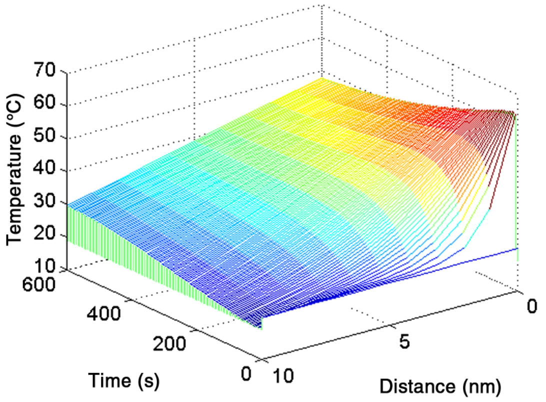

Fig. 11 Calculated temperature profile over time through the partition thickness.

[Eqs. (2)–(6)]. Though the analytical model does not accurately predict the temperature gradient during this region of the finite element model, the effect on the wall temperatures calculated by the analytical model was minor since the convection along the walls is the dominant source of heat transfer in the model.

4.3 *T-Matrix and Modified T-Matrix Models*

The temperature output from the ANSYS model was input into the T-matrix method. The T-matrix method is a computationally fast technique used to approximately solve the coupled mode equations in an optical fiber at the location of an index refraction perturbation (such as at an FBG). The T-matrix method can be applied to calculate the reflected spectrum of an FBG given a nonuniform period change in the refractive index along the FBG, by reducing the grating into piecewise constant approximations.[18] The T-matrix method was modified by Prabhugoud and Peters to include the strain gradient into the calculation of each FBG segment and therefore properly incorporate the effect of large strain gradients.[19] In this modified method, the effective period, $\tilde{\Lambda}$, of the i'th segment is defined as

$$\tilde{\Lambda}_i = \Lambda_o\left[1 + (1 - p_e)\varepsilon(z) + (1 - p_e)z\frac{\mathrm{d}\varepsilon}{\mathrm{d}z}(z)\right]\Bigg|_{z=z_i}, \tag{15}$$

where Λ_o is the initial period of the FBG, p_e is the strain-optic coefficient, $\varepsilon(z)$ is the applied strain, and z is the distance along the FBG segment. The effective period is evaluated at the midpoint of the segment, $z = z_i$. The term modified segment period is used because it is not the actual segment period after deformation, but is an equivalent segment period that produces the same spectrum as solving the coupled mode equations directly in the presence of a strain gradient.

For a free sensor under a temperature load, varying along the length of the FBG, as present in the FBG bandwidth experiment, we can write an equation equivalent to Eq. (15):

$$\tilde{\Lambda}_i = \Lambda_o\left[1 + (\alpha + \beta)\Delta T(z) + (\alpha + \beta)z\frac{\mathrm{d}\Delta T}{\mathrm{d}z}(z)\right]\Bigg|_{z=z_i}, \tag{16}$$

where ΔT is the temperature change in each segment, α is the coefficient of thermal expansion for silica, and β is the thermo-optic coefficient for the FBG. For these simulations, the value of α was 0.55×10^{-6}°C and the value of β is dependent on temperature. For an FBG, β is calculated using the following equation:[15]

$$\beta = \frac{1}{n_{\mathrm{eff}}}\xi, \tag{17}$$

n_{eff} is the effective refractive index of the fundamental mode in the optical fiber and for the FBG used is equal to 1.482. ξ is the thermo-optic coefficient of silica as defined by the following equation:[20]

$$\xi = (-3.6422 \times 10^{-11}{}^{\circ}\mathrm{C}^{-2})T^2 + (1.9619 \times 10^{-8}{}^{\circ}\mathrm{C}^{-1})T + 7.896 \times 10^{-6}. \tag{18}$$

The effective grating period due to applied temperature, $\tilde{\Lambda}$, is used to calculate the general "dc" self-coupling coefficient, $\hat{\sigma}$, as defined by Eq. (19) and the "ac" coupling coefficient, κ, defined by Eq. (20), both as a function of λ, the wavelength of the propagating lightwave:

$$\hat{\sigma}_i = \frac{2\pi}{\lambda}\left(n_{\mathrm{eff}} + \overline{\delta n_{\mathrm{eff}}}\right) - \frac{\pi}{\tilde{\Lambda}_i}, \tag{19}$$

$$\kappa = \frac{\pi}{\lambda}\nu\overline{\delta n_{\mathrm{eff}}}, \tag{20}$$

$\overline{\delta n_{\mathrm{eff}}}$ is the "dc" index change of the optical fiber over the grating period and ν is the fringe visibility. The "ac" and "dc" coupling coefficients are then input into the components of the optical T-matrix, F_i:

$$F_i = \begin{bmatrix} \cosh(\gamma_B\Delta z) - i\frac{\hat{\sigma}_i}{\gamma_B}\sinh(\gamma_B\Delta z) & -i\frac{\kappa}{\gamma_B}\sinh(\gamma_B\Delta z) \\ \frac{\kappa}{\gamma_B}\sinh(\gamma_B\Delta z) & \cosh(\gamma_B\Delta z) + i\frac{\hat{\sigma}_i}{\gamma_B}\sinh(\gamma_B\Delta z) \end{bmatrix}, \tag{21}$$

where Δz is the segment length and γ_B is calculated as

$$\gamma_B = \sqrt{\kappa^2 - \hat{\sigma}_i^2}. \tag{22}$$

The optical T-matrix, F, for the entire FBG is assembled by the multiplication of the optical T-matrix for each segment. The total F is then applied to calculate the amplitudes of the forward- and backward-propagating modes in the fiber, $R(z)$ and $S(z)$, respectively:

$$\begin{bmatrix} R\left(\frac{-L}{2}\right) \\ S\left(\frac{-L}{2}\right) \end{bmatrix} = F\begin{bmatrix} R\left(\frac{L}{2}\right) \\ S\left(\frac{L}{2}\right) \end{bmatrix}, \tag{23}$$

L is the length of the FBG, where the midpoint of the grating is located at $L = 0$. Over a wide wavelength range, with constant reflectivity of 1, the known boundary conditions for the FBG are the forward-propagating mode input, $R[(-L)/2] = 1$, and the backward-propagating mode input, $S(L/2) = 0$. From these boundary conditions, the reflectivity of the FBG as a function of wavelength can be calculated as the amplitude of the output propagating mode divided by the input forward-propagating mode:

$$r(\lambda) = \left|\frac{S\left(\frac{-L}{2}\right)}{R\left(\frac{-L}{2}\right)}\right|^2 = \left|S\left(\frac{-L}{2}\right)\right|^2. \tag{24}$$

The modified T-matrix method does not account for apodization in the grating, which can suppress the presence of side lobes in the fringes of the spectrum. The fringe visibility, ν, is the input parameter to the T-matrix and modified T-matrix methods that have the dominant effect on the presence of side lobes, as well as the intensity of the spectrum. When simulating the FBG spectrum, the input of ν was such that the intensity of the simulated initial spectrum matched the intensity of the experimentally observed initial spectrum.

5 Numerical Simulation Results

The initial simulated spectrum as determined by the T-matrix and modified T-matrix methods is shown in Fig. 12 along with the measured initial spectrum. The values of the FBG properties used in the T-matrix and modified T-matrix methods are given in Table 4.

The initial simulated spectrum produced a good fit to the initial experimental spectrum. As there is no applied temperature gradient, the T-matrix and modified T-matrix simulations (plotted in Fig. 12 as crossed and dashed lines) are identical. The FWQM bandwidth for each numerically determined spectrum calculated by the numerical model was also determined. In addition to broadening, the shape of the numerically calculated spectra contains significant side lobes not observed in the experimental data. As small changes to these side lobes can significantly change the FWQM, a first-order Gaussian fit was applied to each spectrum to smooth the numerical spectra:

$$f(x) = a \times \exp\left[-\frac{(x-b)^2}{c}\right], \tag{25}$$

where a, b, and c are the coefficients from the Gaussian fit. The Gaussian fits for the modified T-matrix compared with the raw simulated spectra and the experimental spectra are shown in Fig. 13. This figure shows that the Gaussian fit of the T-matrix method calculated spectrum is similar in shape to the experimentally observed spectrum, though the wavelength shift of the spectrum is less.

The bandwidth over time of the spectra calculated by the T-matrix and modified T-matrix methods, smoothed with the Gaussian fit, is compared with the experimental data in Fig. 14. The FWQM bandwidth of the modified T-matrix method calculated spectra fits the experimental data well. The FWQM bandwidth of the numerically calculated spectra fits the experimentally observed bandwidths extremely well. The bandwidth of the spectra calculated by the T-matrix method underestimates the experimental bandwidth, and this agrees with comparisons between experimentally observed spectra and spectra calculated by the T-matrix method under a pure strain gradient.[19]

Figure 15 shows that the largest deviation between the experimental and modified T-matrix method calculated bandwidths in the initial 100 s, when the temperature gradient calculated by the finite element model was the least linear. Incorporating the thermal gradient into the T-matrix method is important. Further, the FBG may be apodized to reduce the side lobes, slightly affecting the bandwidth response. However, the thermal gradient is clearly of sufficient magnitude to create the experimentally measured FWQM changes. Figure 15 shows the bandwidths calculated

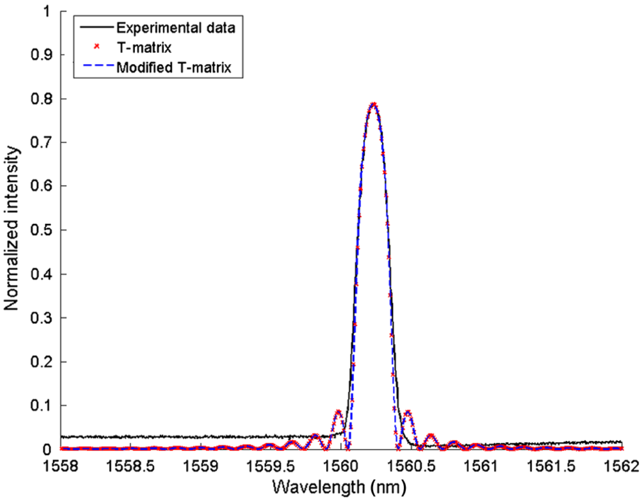

Fig. 12 Initial experimental spectrum of FBG 2 compared with the simulated spectra from the T-matrix and modified T-matrix methods.

Table 4 FBG properties used in the T-matrix and modified T-matrix methods.

FBG property	Value
Length	10^7 nm (1 cm)
Refractive index (n)	1.482
Coefficient of thermal expansion (α)	0.55×10^{-6} m/°C
Initial Bragg wavelength (λ)	1560.4 nm
Fringe visibility (ν)	2.8
"dc" index change ($\overline{\delta n_{\mathrm{eff}}}$)	0.5×10^{-4}

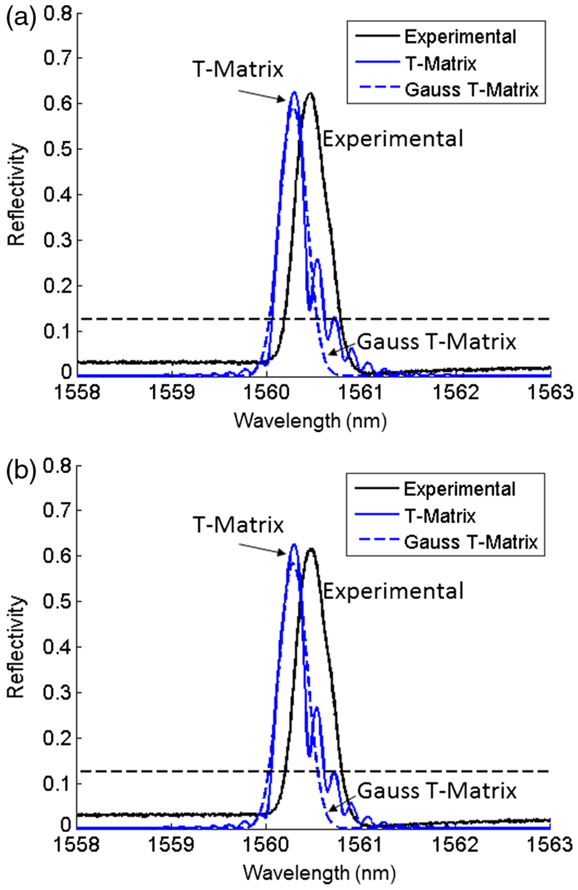

Fig. 13 Simulated reflected spectra given by the modified T-matrix method along with the first-order Gaussian fit for the data at (a) 20 s and (b) 25 s as calculated from temperature data given by the ANSYS model. The dashed line shows the location of the FWQM bandwidth.

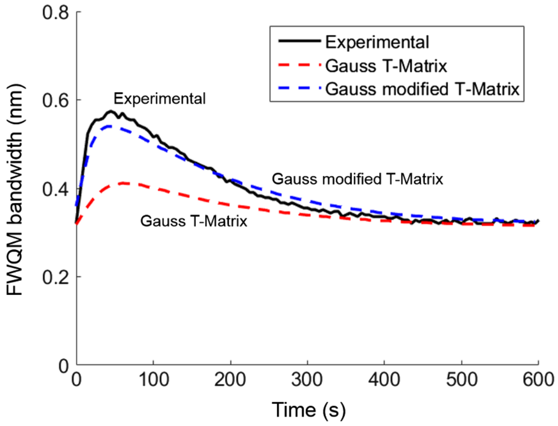

Fig. 14 Comparison of the Gaussian fit of the T-matrix and modified T-matrix spectra FWQM bandwidth with experimental spectrum FWQM bandwidth.

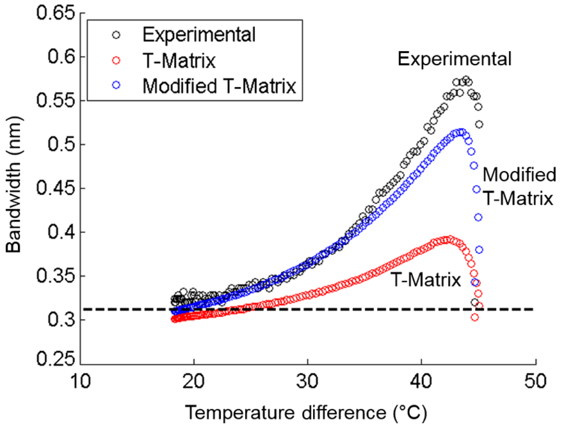

Fig. 15 Values for the FWQM bandwidth given by the T-matrix and modified T-matrix methods plotted as a function of temperature difference between the numerically calculated values for T_{hw} and T_{cw}.

by the T-matrix and modified T-matrix methods, as well as the bandwidth of the experimentally observed spectrum, as a function of the numerically calculated temperature difference between the walls. For the experimental data in Fig. 15, the calculated wall temperatures were used to determine the temperature difference rather than the bath temperatures as seen in Fig. 6.

As the simulation progresses, the spectra determined by the modified T-matrix method become almost identical to the spectra determined by the T-matrix method. After 450 s, the Gaussian fit bandwidths are indistinguishable from the experimental bandwidths and the temperature difference between the hot and cold walls is 21.5°C. As can be seen in Fig. 11, the temperature profile through the ANSYS modeled FBG was nearly linear.

A third-order fit was also applied to the modified T-matrix curve in Fig. 15 when the temperature difference between the walls was between 15°C and 40°C:

$$\delta T = \left(5174\frac{^\circ\mathrm{C}}{\mathrm{nm}^3}\right)(\delta\lambda)^3 - \left(1871\frac{^\circ\mathrm{C}}{\mathrm{nm}^2}\right)(\delta\lambda)^2 + \left(300.3\frac{^\circ\mathrm{C}}{\mathrm{nm}}\right)(\delta\lambda) + 18.58^\circ\mathrm{C}, \tag{26}$$

where δT is the magnitude of the temperature difference and $\delta\lambda$ is the change in bandwidth. This temperature range excludes the initial development of the bandwidth change and captures only the decay of the bandwidth change.

6 Conclusions

The thermal bath experiment presented in this work successfully demonstrated the effect of a controlled thermal gradient on FBG spectrum response. The FBG located within the partition between the baths showed significant sensitivity to the thermal gradient created by the differing temperatures of the baths. The FWQM proved to be a good bandwidth measure across the temperature range and nearly doubled due to a gradient with a magnitude less than 100°C/cm. The experimental results were also compared with a numerical model consisting of a 2-D heat transfer model of the entire system, a detailed finite element model of the heat transfer through the partition, and a T-matrix prediction of the FBG spectral response.

The bandwidths of the numerically determined spectra matched the bandwidths of the experimentally observed spectra well, though the model did underestimate the Bragg wavelength shift of the spectra. The numerical model showed that the sensitivity of an FBG to a temperature gradient was more significant than what was experimentally observed because the experimental data relied on the larger temperature difference between the baths. According to the numerical model, an FWQM bandwidth change of 0.25, nearly double the initial bandwidth, is due to only a 32°C temperature difference over the length of the FBG. Most importantly, the simulations confirmed that the observed FWQM changes were consistent with the magnitude of the applied thermal gradients.

Acknowledgments

Funding for this research has been provided as a subcontract from Intelligent Fiber Optic Systems Inc. (IFOS) via NASA Contract Numbers NNX11CI02P (Phase 1) and NNX12CB01C (Phase 2).

References

1. P. C. Hill and B. J. Eggleton, "Electrically tunable power efficient dispersion compensating fiber Bragg grating," *IEEE Photonics Technol. Lett.* **11**, 854–856 (1994).
2. K. S. C. Kuang et al., "Residual strain measurement and impact response of optical fiber Bragg grating sensors in fibre metal laminates," *Smart Mater. Struct.* **10**, 338–346 (2001).
3. K. S. C. Kuang et al., "Embedded fibre Bragg grating sensors in advanced composite materials," *Compos. Sci. Technol.* **61**, 1379–1387 (2001).
4. S. Minakuchi, Y. Okabe, and N. Takeda, "Real-time detection of debonding between honeycomb core and facesheet using a small diameter FBG sensor embedded in adhesive layer," *J. Sandwich Struct. Mater.* **9**, 9–33 (2007).
5. D. Hackney and K. Peters, "Damage identification after impact in sandwich composites through embedded fiber Bragg sensors," *J. Intell. Mater. Syst. Struct.* **22**, 1305–1316 (2011).
6. R. J. Black and B. Moslehi, "Advanced end-to-end fiber optic sensing systems for demanding environments," *Proc. SPIE* **7817**, 78170L (2010).
7. R. J. Black et al., "Fiber optic temperature profiling for thermal protection heat shields," *Proc. SPIE* **9062**, 906204 (2014).
8. R. J. Black et al., "Fiber optic temperature profiling for TPS heat shields," *Opt. Eng.* **55**(11), 114101 (2016).
9. A. Little et al., "The Mars Science Laboratory (MSL) entry, descent and landing instrumentation (MEDLI): hardware performance and data reconstruction," in NASA Preprint AAS-13-078, NF1676L-15960 (2013).

10. J. M. Costa et al., "Advances in high temperature fiber optic sensors for turbine engine applications," in *Proc. 58th Int. Instrumentation Symp. (IIS)*, San Diego (2012).
11. J. Lauzon et al., "Implementation and characterization of fiber Bragg gratings linearly chirped by temperature gradient," *Opt. Lett.* **19**, 2027–2029 (1994).
12. Z. Chen et al., "Tunable chirped fiber Bragg gratings by a distributed heater," *Opt. Eng.* **40**, 1156–1157 (2001).
13. B. J. Eggleton et al., "Electrically tunable power efficient dispersion compensating fiber Bragg grating," *IEEE Photonics Technol. Lett.* **11**, 854–856 (1999).
14. J. A. Rogers et al., "Distributed on-fiber thin film heaters for Bragg gratings with adjustable chirp," *Appl. Phys. Lett.* **74**, 3131–3133 (1999).
15. D. Hackney, "Characterization of fiber Bragg gratings as thermal sensors in complex environments," Dissertation, North Carolina State University (2015).
16. A. Bejan, *Heat Transfer*, John Wiley & Sons, New York (1993).
17. Y. S. Touloukian, *Thermal Expansion: Nonmetallic Solids*, IFI/Plenum, New York (1977).
18. M. Yamada and K. Sakuda, "Analysis of almost-periodic distributed feedback slab waveguides via a fundamental matrix approach," *Appl. Opt.* **26**, 3474–3478 (1987).
19. M. Prabhugoud and K. Peters, "Modified transfer matrix formulation for Bragg grating strain sensors," *J. Lightwave Technol.* **22**, 2302–2309 (2004).
20. D. B. Leviton and J. F. Frey, "Temperature-dependent absolute refractive index measurements of synthetic fused silica," *Proc. SPIE* **6273**, 62732K (2006).

Drew A. Hackney received his PhD in mechanical engineering from North Carolina State University in 2015. Currently, he is employed at North Carolina State as a postdoctoral research scholar where his research specializes in fiber optic sensors under dynamic loads.

Kara J. Peters received her PhD in aerospace engineering from the University of Michigan in 1996. Until 2000, she was a research collaborator at the Ecole Polytechnique Fédérale de Lausanne, Switzerland, in the Laboratory of Applied Mechanics and Reliability. In 2000, she joined the faculty of the Department of Mechanical and Aerospace Engineering at North Carolina State University, where she is currently a professor and conducts research on optical fiber sensors.

Richard J. Black received his PhD in fiber optics from the Australian National University. He is a founding member and the chief scientist at Intelligent Fiber Optic Systems Corporation (IFOS). He was an invited professor at the Ecole Polytechnique Fédérale de Lausanne and a research fellow at the Ecole Polytechnique de Montréal. His research interests include photonic components and sensing systems with application to aerospace and energy systems, robotics and medical devices.

Joannes M. Costa: Biography is not available.

Behzad Moslehi received his PhD in electrical engineering from Stanford University. He is the founder and CEO/CTO of IFOS. Previously, he was with Optivision/ONI Systems (acquired by Ciena), Physical Optics Corporation (POC), Litton and Xerox. His current research interests include photonic signal processing, sensing, communications, and networking for applications in aerospace, safety, life sciences, and energy.